Chapter 8

Forward Cross-sections

8.1 Definition and calculation

What is the probability of a collision when a spherical projectile of diameter D_P impinges on a sheet of sparsely-packed spherical targets of diameters D_T? Classically, the answer is simply the product of the number of targets per area multiplied by the *effective* cross-section of one target. Because the projectile has finite size, we can see schematically (Fig. 8.1) that the cross-sectional area about the center of a given target in which a collision will result if entered by the center of a projectile is a circle of diameter $D_{int} = D_P + D_T$. The subscript "*int*" underscores the fact that the effective cross-section is a property of the interaction, that is, of both target and projectile, rather than the target alone.

This concept, the cross-section of an interaction (denoted σ), can usefully be extended to quantify the likelihood of *any* interaction between colliding particles. Here, we are concerned with the cross-section of charm meson production in high-energy collisions of various charged hadrons on a fixed target composed of a variety of nuclear materials. Although wave-particle duality and the presence of long-range forces complicates the interpretation of the total cross-section for interaction between two particles in terms of their physical sizes, in the case of hadronic collisions, where strong interactions dominate, this picture remains essentially valid. Due to color confinement, the strong interaction is at low energy scales effectively mediated not by

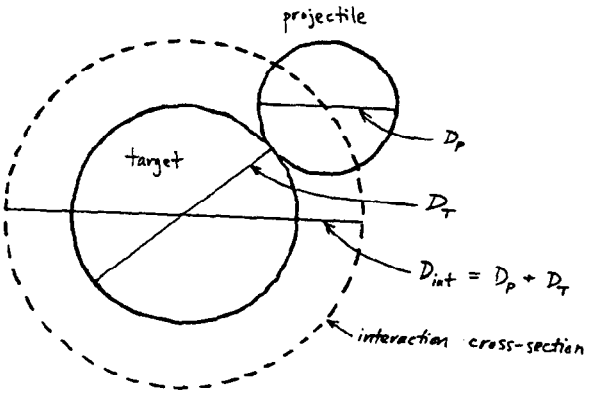

Figure 8.1: Classical cross-section for a collision of two spheres.

the massless gluon but rather by the massive pion. Therefore, the pion mass (~140 MeV) sets the distance scale of strong bonds between color-neutral states at around a fermi. Barring some exotic deconfined state such as quark-gluon plasma, this distance scale will also correspond to the sizes of the hadrons themselves. Take, for example, the total cross-section for pp scattering (elastic plus inelastic) at E769's beam energy, measured to be approximately 40 mb [35]. Solving for the diameter of the proton, we obtain

$$D = \sqrt{\frac{\sigma(pp)}{\pi}} = \sqrt{\frac{40\,\mathrm{mb}}{\pi}} = \sqrt{\frac{40 \times 10^{-27}\,\mathrm{cm}^2}{\pi}} \simeq 1\,\mathrm{fm}, \tag{8.1}$$

which corresponds to measures of nucleonic[1] size obtained by other means.

In the above discussion, we have not addressed the issue of composite targets, such as nuclei, which are roughly-spherical bound states of some number (the atomic mass A) of nucleons. For many processes, the per-nucleus cross-section can be parametrized by the following power law:

[1]The near equality of the total pp and pn cross-sections indicates that protons and neutrons are of the same size, in keeping with isospin symmetry.

$$\sigma_A = \sigma_0 A^\alpha, \tag{8.2}$$

where σ_0 is a constant. Assuming the volume of a nucleus is proportional to A, the "physical" cross-section of the nucleus should be governed by an $\alpha = 2/3$ dependence. In fact, for nucleon-nucleus scattering, $\alpha \simeq 0.7$ [35]. At high momentum transfers, however, we expect the effect of "nuclear shadowing" to diminish for particular hadronic processes as the distance scale of the interaction decreases; in this case, the projectile "sees" nucleons rather than nuclei (and ultimately partons rather than nucleons). In this limit, the nucleus comes to look more and more like a loosely-packed collection of individual nucleonic targets, leading to a linear dependence of the per-nucleus cross-section on A (i.e., $\alpha = 1$). E769 has published measurements of α for both pseudoscalar and vector D production; α in both cases is found to be consistent with unity [7, 9].

The per-nucleon cross-section σ_N is simply related to σ_A:

$$\sigma_N = \frac{\sigma_A}{A} = \sigma_0 A^{\alpha-1} \tag{8.3}$$

For linear A-dependence (which we assume in all that follows), σ_N is constant. We now drop the subscript "N"; all cross-section measurements reported in this thesis are to be understood as cross-sections per nucleon.

Forward cross-sections are determined for each beam particle/beam energy combination present in the data. Since beam polarity, beam energy, DISC pressure setting, and trigger logic all varied one or more times at different points within the experimental running, each of these combinations is naturally associated with a particular subset of E769 events. These subsets are characterized by the run region(s) during which the events were collected and the trigger type(s) under which the events were written to tape. In Section 6.2, these parameters, as well as the beam particle flux (defined below), are tabulated for each data subset. In the following equations, extensive quantities (e.g., number of D events) are understood to be time-integrated (operationally, spill-integrated) sums over the appropriate run region(s); intensive quantities (e.g., trigger efficiency) are understood to be flux-weighted averages over

the same run region(s) unless they are constant or an alternate method of averaging is explicitly described.

The cross-section for inclusive forward production of a particle D in B-nucleon collisions is given by

$$\sigma(BN \rightarrow DX) = \frac{N_{prod}(B,D)}{F(B)\ T_N}. \tag{8.4}$$

In this equation,

$N_{prod}(B,D)$ = number of D's produced through B-target collisions,
$F(B)$ = number of B's incident on the target during the detector's livetime, and
T_N = nucleons/area in the target.

Rather than define the cross-section as a ratio of particle production rates to incident luminosities, we use the equivalent time-integrated quantities. N_{prod} refers to particles produced in the forward hemisphere in the center-of-mass frame of the interaction (i.e., $x_F > 0$); it is given by

$$N_{prod}(B,D) = \frac{N_{obs}(B,T,D \rightarrow xyz)}{B(D \rightarrow xyz)\ \epsilon_{geom}(D \rightarrow xyz)\ \epsilon_{beamID}(B)\ \epsilon_{trig}(T, D \rightarrow xyz)}. \tag{8.5}$$

In this equation,

$N_{obs}(B,T,D \rightarrow xyz)$ = number of D's ($x_F > 0$) observed through invariant mass reconstruction of decay $D \rightarrow xyz$ in events passing trigger T and with positive identification of B,
$B(D \rightarrow xyz)$ = branching fraction for decay $D \rightarrow xyz$,
$\epsilon_{geom}(D \rightarrow xyz)$ = efficiency for observing D ($x_F > 0$) through invariant mass reconstruction of decay $D \rightarrow xyz$,
$\epsilon_{beamID}(B)$ = efficiency for positive identification of B, and
$\epsilon_{trig}(T, D \rightarrow xyz))$ = efficiency for event containing $D \rightarrow xyz$ to pass trigger T.

Decay mode	$B(\%)$
$D^+ \to K\pi\pi$	9.1 ± 0.6
$D^0 \to K\pi$	4.01 ± 0.14
$D_s \to \phi\pi$	3.5 ± 0.4
$\phi \to K^+K^-$	49.1 ± 0.9
$D_s \to K^*K$	3.3 ± 0.5
$K^* \to K^-\pi^+$	$2/3 \times 100$ [a]
$D_s \to KK\pi_{res}$ [b]	3.92 ± 0.39
$D^* \to D^0\pi$	68.1 ± 1.3

[a] Derived from isospin analysis.
[b] Defined as sum of $\phi\pi$ and K^*K contributions to $KK\pi$.

Table 8.1: 94 PDG branching fractions.

In Table 8.1, 94 PDG branching fraction values for the relevant decay modes are listed.

We do not expect the efficiency for tagging a B to depend on whether charm is produced in the event. Therefore, we connect $F(B)$ to its tagged counterpart via the quantity $\epsilon_{beamID}(B)$ defined above:

$$F(B) = \frac{F_{ID}(B)}{\epsilon_{beamID}(B)}, \tag{8.6}$$

where $F_{ID}(B)$ is the number of positively-identified B's incident on the target during the detector's livetime (hereafter called the "B flux").

As described in Section 3.2, beam-particle identification is a two-step process. During spills in which the DISC pressure is set to identify either π, K, or p, a four-fold coincidence from the DISC (with at least one hit in each quadrant) is sufficient to identify the beam particle. If the DISC does not fire or is not set to identify any particular beam particle, however, additional information is required. In the negative running, this information is simply the *a priori* beam probabilities, which indicate that there is a greater than 90% chance that an unidentified beam particle is a π^-. In the positive running, this is not the case; the TRD must be used to distinguish pions

from non-pions. If the DISC is set to tag kaons, *a priori* beam probabilities indicate a greater than 90% chance that a non-DISC-tagged non-pion is a proton rather than a kaon.[2] Therefore, $F_{ID}(B)$ can be written

$$F_{ID}(B) = \chi_{att}(B)\ \chi_{empty}\ (F_{DISC}(B) + F_{NDISC}(B)), \tag{8.7}$$

where χ_{att} is a factor which corrects for the attenuation of the beam upstream of and within the target (see Section 3.3) and χ_{empty} is a subset-dependent factor correcting for the presence of anomalously-empty spills (i.e., spills for which the beam intensity is incorrectly recorded as zero).[3] Both of these correction factors are small, on the order of 1-2%.

The above equation is only approximately correct in that it ignores the contamination of the experimentally-tagged B sample by other beam particles. More properly, we should write

$$F_{trueID}(B) = \sum_b C_{bB}\ F_{ID}(b), \tag{8.8}$$

where the sum runs over beam particles and the matrix element C_{bB} gives the % contamination of "B" by b. A similar procedure would have to be carried out for the charm signals N_{obs} as well. In E769, the definition of positive identification of a beam particle is that the probability for a correct tag is greater than or equal to 90%. This puts an upper limit of 10% on the contamination of any tagged sample by other beams; in most instances, however, the contamination is much lower (see Section 3.2 for a full discussion and tabulation of beam contaminations). In this analysis, we forego this correction and simply use the contaminated beam samples. This simplification is justified not only by the typically low levels of contamination but also (after the fact) by the fairly weak dependence of our measured cross-sections (relative to their statistical precision) on beam particle type.

[2]If the DISC is set to tag protons, this is not the case. Therefore, in Region 4 *only* DISC-tagged protons contribute to the identified proton flux.

[3]This "empty-spill" correction is the kind that normally would have been taken care of through event weeding. Therefore, these correction factors are derived in Section 6.1.

Each component of $F_{ID}(B)$ is calculated using scaler[4] information in one of two ways, depending on the method of beam-particle identification. For DISC-tagged B's, the scaler tallying the number of four-fold coincidences in the DISC (N_{DISC}) can be used as a direct count of events. In this case,

$$F_{DISC}(B) = \sum_{i}^{spills} (N_{DISC})_i \; (\epsilon_{live})_i, \tag{8.9}$$

where the sum runs over spills in which the DISC pressure is set to tag B and ϵ_{live} is the detector livetime. Note that in the absolute cross-section analysis, full-weeding of events (including scalers) is required.

The DISC, whose four-fold coincidences are amenable to counting, is included in E769's trigger logic to enhance the number of K and p-induced charm events written to tape. The output of the TRD, on the other hand, consists of multiple signals, up to one from each of its planes. TRD beam probabilities are (run-dependent) functions of the number of planes that fire. Thus, the TRD is not used to trigger events, and no scaler N_{TRD} exists to provide tagged-B totals analogous to N_{DISC}. For non-DISC-tagged B's, fluxes must therefore be calculated from the scaler tally of the total number of beam particles impinging on the target (N_{BEAM}). In this case,

$$F_{NDISC}(B) = f(B) \sum_{i}^{spills} (N_{BEAM})_i \; \epsilon_{NDISC}(B)_i \; (\epsilon_{live})_i, \tag{8.10}$$

where the sum runs over all spills, $f(B)$ is the *a priori* B probability, and $\epsilon_{NDISC}(B)$ is the efficiency for tagging B through means other than the DISC. (Since in the negative running, *all* non-DISC-tagged particles are identified as π^-, the product $f(\pi^-)\,\epsilon_{NDISC}(\pi^-)$ should be taken to equal one.) This equation, however, does not include all of the information that is potentially available, namely the DISC setting and how many times the DISC fired in each spill; it is therefore only applicable for spills in which the DISC is not set to tag anything or is not operational.

The need for a modification in the more general case that the DISC *is* set is made clear by an example. In order to count the number of beam pions in a spill during

[4]See Section 3.6 for a discussion of the scalers used in this analysis.

which the DISC is set to tag kaons, we apply efficiencies to the scaler count only after the positively-identified kaons have been subtracted. The beam probabilities $f(B)$ must therefore also be adjusted in order to reflect the particle fractions in the remaining subset of the beam. These refinements lead to the following equation:

$$F_{NDISC}(B) = \sum_{i}^{spills} (N_{BEAM} - N_{DISC})_i \; f'(B)_i \; \epsilon_{NDISC}(B)_i \; (\epsilon_{live})_i, \tag{8.11}$$

where the sum runs over spills with the DISC set to tag something and $f'(B)$ is the B probability in the absence of a DISC tag, given by

$$f'(B) = \frac{(1 - \delta_{bB}\,\epsilon_{DISC})\,f(B)}{1 - \epsilon_{DISC}\,f(b)}, \tag{8.12}$$

where the DISC is set to b, δ_{bB} is equal to 1 if $b = B$ and equal to zero otherwise, and ϵ_{DISC} is the tagging efficiency of the DISC.[5] (As explained above, $f'(\pi^-)\,\epsilon_{NDISC}(\pi^-)$ should be taken to equal one.) The efficiencies ϵ_{DISC} and ϵ_{NDISC} are discussed in Section 3.2.

The cross-section is given its dimension by the T_N term, given by

$$T_N = N_{AV} \sum_{i}^{mat.} \rho_i \; t_i, \tag{8.13}$$

where the sum runs over the materials comprising the target. In this equation,

N_{AV} = Avogadro's number = 6.022×10^{23},
ρ = mass density in grams/volume, and
t = thickness along the beam direction.

In this analysis, charm particles produced in all 26 target foils (comprised of four materials) as well as in the interaction scintillator are included in the final data samples. The target is described (including the densities and thicknesses of its components)

[5]The DISC efficiency is taken to be independent of B. The systematic error associated with this assumption is discussed in Section 8.2.

in Section 3.3. The simple calculation described above leads to the following result: $T_N = 1.66 \times 10^{-3}$ nucleons/mb.

By defining the acceptance $Acc(T, D \rightarrow xyz)$ as the product of $\epsilon_{geom}(D \rightarrow xyz)$ and $\epsilon_{trig}(T, D \rightarrow xyz)$ (see Section 7.4 for a full discussion), we can now write the cross-section equation in terms of directly-measured quantities:

$$\sigma(BN \rightarrow DX) = \frac{N_{obs}(B, T, D \rightarrow xyz)}{B(D \rightarrow xyz)\ Acc(T, D \rightarrow xyz)\ F_{ID}(B)\ T_N}. \tag{8.14}$$

Forward cross-section results for each beam/particle combination are tabulated in Section 8.3.1. For information regarding the numerical values of the various inputs to the above equation, refer to the relevant sections:

$N_{obs}(B, T, D \rightarrow xyz)$	Section 6.3
$Acc(T, D \rightarrow xyz)$	Section 7.4
$B(D \rightarrow xyz)$	Section 8.1
$F_{ID}(B)$	Section 6.2
T_N	Section 8.1

8.2 Systematic errors

The precision of cross-section measurements is limited by statistical uncertainty (σ_{stat}) in the number of events seen N_{obs}; in most cases, although analysis cuts have been optimized to maximize the statistical significance of the D signals, σ_{stat} remains the dominant contribution to the overall error. As described in Section 6.3, signal estimates are obtained through log-likelihood fits. The standard (or "1σ") error on a fit parameter (such as the number of signal events) is returned by the fitter on the basis of how variations in that parameter affect the quality of the fit, in this case quantified by the log-likelihood function. Although the details of the fitting procedure may differ, ultimately the statistical error on the number of signal events is determined through Poisson statistics by the numbers of signal and background events in the invariant mass range corresponding to a given particle decay; σ_{stat} is therefore

separated from errors which arise from other sources, such as procedural choices in the analysis or lack of precise knowledge of experimental conditions. These latter errors are called "systematic" and are discussed in this section; statistical errors are compiled in Section 6.3.

The total systematic error on a cross-section is given by the systematic errors on the data signal, acceptance, and flux, where these independent contributions are added in quadrature. (Errors in the cross-sections due to uncertainty in the branching fractions of decay modes are listed separately from errors contingent upon E769-specific details.) In comparing two cross-section results, it is important to know which components of their respective systematic errors are common to both and which are independent. Systematic errors of the forward cross-sections are usefully divided into two categories: those which depend on the data subset and those which do not. In reporting cross-sections, the systematic errors will be split along this line. While this allows for convenient calculation of the appropriate common systematic error for a comparison of, say, D^+ cross-sections for production induced by different beams, a different comparison, for example between π-induced D^+ and D^0 cross-sections, will require a different partitioning of systematic errors. In the following subsections, the reader will be given enough information to derive the systematic error appropriate to any given comparison of forward cross-section results. Note that these systematic errors are tabulated as *relative* errors on the relevant quantities.

8.2.1 Data signals

In addition to the statistical error on N_{obs} mentioned above, a systematic error on this quantity, attributable to choices made in the fitting procedure, can be estimated. Two potential contributions to this error were examined, namely, uncertainty in the data signal estimates due to the fixed widths and fixed central masses chosen. As described in Section 6.3, widths are fixed to floating values obtained by fits to the total simply-weeded signals and masses are fixed to 94 PDG values. The mean change in the signal estimate due to fixing these quantities at $\pm 1\sigma$ from the central value is taken to be the systematic error. Errors associated with the fixed signal width are listed in Table 8.2; no significant error arises from the uncertainties in the PDG

masses, which are known to better than 1 MeV.

Data subset	D^+	D^0	D_s	D^*
Reg. 1 π^-	2.4%	2.3%		
Reg. 2 π^-	2.0%	2.3%	5.5%	2.7%
Reg. 1 K^-	2.4%	1.6%		
Reg. 2 K^-	1.3%	2.0%	2.5%	.9%
π^+	1.9%	3.1%	4.5%	2.9%
K^+	1.6%	3.1%	2.4%	4.4%
p	1.9%	3.2%	8.9%	5.7%

Table 8.2: Systematic errors on data signal estimates due to uncertainty in fixed data signal width.

8.2.2 Acceptance

As described in Section 7.4, the systematic error on acceptances due to statistical error in the MC signals are determined using unweighted MC for each species. These errors are given in Table 8.3. In addition to these, there are systematic errors associated with each of the MC weighting functions used (or in the case of the Čerenkov efficiency correction, *not* used) in the absolute cross-section analysis.

Beam polarity	D^+	D^0	D_s	D^*
negative	1.0%	1.1%	1.7%	1.8%
positive	1.2%	1.2%	2.1%	2.2%

Table 8.3: Systematic errors on acceptance due to MC statistics.

The errors associated with the drift chamber efficiency correction factors χ_{DC} (see Section 7.2.5) are derived from MC statistics in the same way as those listed above,

except that the overall error is obtained by propagating the errors on each of the acceptances in the flux-weighted average corresponding to a given run region. These errors are listed in Table 8.4. Because χ_{DC} is derived using D^+ MC, the treatment of errors for this particle differs from that for the remaining species (see footnotes in Table 8.4).

Data subset	$F_{prod}(x_F)$	$F_{prod}(p_T^2)$	ϵ_{trig}	χ_{DC}	total σ_{syst}
Reg. 1 or 2 π^-	0.2%	0.9%			
Reg. 1 π^-			0.7%	—	1.2%
Reg. 2 π^-			1.0%		1.4%
Reg. 1 or 2 K^-	0.4%	1.6%			
Reg. 1 K^-			0.2%	—	1.7%
Reg. 2 K^-			0.1%		1.7%
π^+	0.1%	1.2%	1.0%	0.7% (1.4%)[a]	5.2% (5.3%)[b]
K^+	0.1%	1.7%	0.1%	0.7% (1.4%)	1.8% (2.2%)
Reg. 3 p			1.0%	0.7% (1.4%)	
Reg. 4 p			0.5%	1.0% (1.5%)	
Reg. 3+4 p	1.2%	2.2%			6.3% (6.4%)

[a] For D^+, the error on the DC efficiency correction factor *replaces* the error due to MC statistics. For other particles, the DC efficiency error in parentheses is *added in quadrature* to the MC statistical error.

[b] Total systematic errors in parentheses are for particles other than D^+.

Table 8.4: Data subset-dependent systematic errors on acceptance. $F_{prod}(x_F)$ and $F_{prod}(p_T^2)$ errors for D^* are calculated separately.

Up to this point, the systematic errors have been calculated using standard error propagation for a function of one or more independent variables. In the cases of differential distribution and trigger efficiency weighting, however, the function (here, the acceptance) depends on a number of correlated variables, namely the parameters returned by some fit. In order to take these correlations into account correctly, we use the following formula:

$$\sigma_{syst}(Acc) \equiv \sqrt{\overline{\sigma^2(Acc)}} = \sqrt{\sum_i (\frac{\partial Acc}{\partial x_i}\ \sigma(x_i))^2 + 2 \sum_{i>j} \rho_{ij}\ \frac{\partial Acc}{\partial x_i}\ \frac{\partial Acc}{\partial x_j}\ \sigma(x_i)\ \sigma(x_j)}, \tag{8.15}$$

where the sum runs over a set of correlated variables x, ρ_{ij} is the correlation coefficient for x_i and x_j (an element of the error matrix returned by MINUIT), and $\sigma(x_i)$ is the 1σ variation in x_i.

The systematic errors associated with differential distribution weighting are not expected to depend strongly on the charm species. Therefore, D^+ MC is used to determine this error for all species except D^*, for which these errors are separately calculated. Similarly, errors associated with trigger efficiency weighting were also found using D^+. Both of these contributions to the systematic error on acceptance are given in Table 8.4; see Table 8.5 for the D^* systematic errors. In all cases, these weighting errors prove to be relatively small components of their respective total systematic errors.

Data subset	$F_{prod}(x_F)$	$F_{prod}(p_T^2)$	total σ_{syst}
π/K	1.5%	1.5%	2.1%
p	3.6%	0.9%	3.7%

Table 8.5: Systematic errors on D^* acceptance due to differential distribution weighting.

As discussed in Section 7.2.2, no Čerenkov efficiency weighting was implemented in the absolute cross-section analysis. The uncertainty in the data-determined efficiency is used, however, to calculate a contribution to the overall systematic error on acceptance. Here the independent parameters which are adjusted are the Čerenkov efficiencies in each bin of p_K. After summing in quadrature the effect of these variations, the total systematic error due to uncertainty in the Čerenkov kaon identification efficiency is found to be 4.2%. Note that this is the error for one kaon decay product; therefore, this systematic error is doubled for the D_s modes. Clearly, this error

dominates the systematic uncertainty on acceptance.

In Table 8.6, the acceptance uncertainties associated with the errors in the 94 PDG average lifetime values are given; these were measured by varying the lifetimes (via weighting) by $\pm 1\sigma$ and noting the effect on acceptance. The relative errors on acceptance were found to go as those on the lifetimes themselves, multiplied by 150%, independent of data subset.

Particle	$F_{\tau dist.}$
D^+	1.2%
D^0	1.4%
D_s	5.5%
D^*	1.2%

Table 8.6: Systematic errors due to lifetime weighting.

8.2.3 Flux

Of the factors that go into the calculation of live flux, only ϵ_{live}, $f'(\pi^+)$, and $f'(p)$ are found to have significant systematic errors associated with them. Due to the large numbers involved, the raw flux totals obtained from scaler sums have no appreciable statistical errors. By weeding out of the absolute cross-section analysis spills for which these scalers are missing or pathological in some way, large systematic errors are also avoided; this weeding is described in Section 6.1. In the positive running, another potential source of systematic error is ϵ_{NDISC} (here, ϵ_{TRD}). Again, because high-statistics fits are used to determine TRD beam probabilities as a function of the number of TRD planes which fire (see Section 3.2), no significant contribution to the systematic error on the positive fluxes arises.

As detailed in Section 3.6, the detector livetime is calculated as a ratio of scalers, specifically the ratio of the scaler downstream of the PLU counting prescaled interaction triggers to the corresponding upstream scaler. Since the PLU is disabled while

the DA system is busy with an event, this ratio provides a high-statistics measure of ϵ_{live}. This procedure for measuring livetime is not the only one possible; an alternative is to take the ratio of scalers at the end and beginning of the strobe stream leading into the PLU, which is disabled during deadtime by the absence of a strobe input signal. One would expect these two measures of livetime to be the same. An average discrepancy of about 1.5%, however, was found between the two. This is taken as an estimate of the systematic uncertainty in ϵ_{live}, which contributes to the total systematic error on the flux.

In the negative running, where beam particle identification proceeds using DISC information or by default in the absence of same, the *a priori* beam probabilities do not come into the flux calculation. As detailed in Section 8.1, these beam fractions (or more precisely, their modified counterparts $f'(\pi^+)$ and $f'(p)$) are needed to determine non-DISC-tagged fluxes in Region 3. Although uncertainty in the DISC-tagging efficiency does lead to uncertainties in these quantities, this contribution is negligible compared to that arising from the intrinsic uncertainties in $f(\pi^+)$ and $f(p)$ themselves. These *a priori* beam probabilities are determined from fits to DISC pressure curves (see Section 3.2), with relative uncertainties of 4.9% and 8.8%, respectively.

8.2.4 Summary

In Table 8.7, total E769-dependent (everything excluding the branching fraction errors) systematic errors are given for each data subset/charm species combination. Note that these errors are correlated with one another to some degree both vertically and horizontally within the table. In addition to these, uncertainties in the 94 PDG branching fractions for the relevant modes contribute the following relative errors into the forward cross-section results: 6.6% for D^+, 3.5% for D^0, 9.9% for D_s, and 4.0% for D^*.

Data subset	D^+	D^0	D_s	D^*
Reg. 1 π^-	5.5%	5.4%		
Reg. 2 π^-	5.3%	5.5%	11.5%	6.3%
Reg. 1 K^-	5.4%	5.3%		
Reg. 2 K^-	5.2%	5.4%	10.8%	5.9%
π^+	7.4%	7.7%	12.7%	8.1%
K^+	5.1%	6.1%	10.8%	7.1%
p	7.9%	8.7%	15.1%	10.0%

Table 8.7: Total E769-dependent systematic errors.

8.3 Results

8.3.1 Forward cross-sections

The results for absolute forward production cross-sections, the calculation of which was outlined in Section 8.1, are tabulated here (Tables 8.8-8.11) for each beam particle/charm meson combination. For D^+ and D^0, 210 GeV beam energy results are given in addition to those at 250 GeV. Four absolute errors are shown for each cross-section value: (1) statistical, (2) data subset-dependent systematic, (3) data subset-independent systematic, and (4) branching fraction. In cases where the data signal has less than a 3σ statistical significance, Bayesian 90% confidence level lower and upper limits are also given.[6] Combined π and K beam weighted averages are calculated.

Over the range in beam energy at which modern fixed-target measurements of charm particle cross-sections have been made (200-800 GeV), $\sigma_{c\bar{c}}$ is expected to rise rapidly; at E769's energy, a rate of increase of about 50% per 100 GeV is predicted. Our 250 (210) GeV results are therefore only directly comparable to those published

[6]The cross-section probability distribution is taken to be a Gaussian with a center and standard deviation as indicated in the tables and the unphysical region below zero excluded. The lower (upper) limit is calculated by finding the boundary of the lower (upper) tail of this distribution whose area is 10% of the total.

B	$\sigma(BN \to D^+X, x_F > 0)$ (μb/nucleon)
π^-	$3.58 \pm 0.23 \pm 0.10 \pm 0.16 \pm 0.23$
	$(1.72 \pm 0.26 \pm 0.05 \pm 0.08 \pm 0.11)$
π^+	$2.58 \pm 0.30 \pm 0.15 \pm 0.12 \pm 0.17$
π	$3.21 \pm 0.18 \pm 0.08 \pm 0.15 \pm 0.21$
K^-	$3.29 \pm 0.68 \pm 0.08 \pm 0.15 \pm 0.22$
	$(3.37 \pm 1.06 \pm 0.10 \pm 0.15 \pm 0.22)$
K^+	$2.90 \pm 0.39 \pm 0.07 \pm 0.13 \pm 0.19$
K	$3.00 \pm 0.34 \pm 0.06 \pm 0.14 \pm 0.20$
p	$3.25 \pm 0.42 \pm 0.21 \pm 0.15 \pm 0.21$

Table 8.8: D^+ forward cross-sections, 250 (210) GeV beam.

B	$\sigma(BN \to D^0X, x_F > 0)$ (μb/nucleon)
π^-	$8.24 \pm 0.70 \pm 0.25 \pm 0.38 \pm 0.28$
	$(6.36 \pm 0.89 \pm 0.18 \pm 0.29 \pm 0.22)$
π^+	$5.71 \pm 0.86 \pm 0.35 \pm 0.27 \pm 0.20$
π	$7.23 \pm 0.54 \pm 0.21 \pm 0.34 \pm 0.25$
K^-	$7.62 \pm 2.07 \pm 0.22 \pm 0.35 \pm 0.26$
	$(4.74 \pm 2.75 \pm 0.12 \pm 0.22 \pm 0.16)$
K^+	$7.07 \pm 1.22 \pm 0.28 \pm 0.33 \pm 0.24$
K	$7.21 \pm 1.05 \pm 0.22 \pm 0.34 \pm 0.25$
p	$5.65 \pm 1.35 \pm 0.41 \pm 0.27 \pm 0.20$

Table 8.9: D^0 forward cross-sections, 250 (210) GeV beam.

by the ACCMOR NA32 collaboration for their 230 (200) GeV π^- and K^- beam runs [17, 19].[7] These results are given in Table 8.12. Considering NA32's relatively low statistics, it is not surprising that our cross-sections are consistent with theirs for each case in which comparison is possible. Note that these and other previous

[7]We limit our comparisons to direct measurements of forward cross-sections (as opposed to extrapolations from more limited x_F ranges).

B	$\sigma(BN \to D_s X, x_F > 0)$ (μb/nucleon)	90% C.L. limits
π^-	$2.11 \pm 0.44 \pm 0.12 \pm 0.21 \pm 0.21$	
π^+	$1.97 \pm 0.61 \pm 0.15 \pm 0.20 \pm 0.19$	
π	$2.06 \pm 0.36 \pm 0.09 \pm 0.21 \pm 0.20$	
K^-	$2.44 \pm 1.36 \pm 0.08 \pm 0.25 \pm 0.24$	$> 0.90, < 4.46$
K^+	$3.35 \pm 0.96 \pm 0.12 \pm 0.34 \pm 0.33$	
K	$3.04 \pm 0.79 \pm 0.08 \pm 0.31 \pm 0.30$	
p	$1.41 \pm 0.85 \pm 0.16 \pm 0.14 \pm 0.14$	$> 0.49, < 2.57$

Table 8.10: D_s forward cross-sections, 250 GeV beam.

B	$\sigma(BN \to D^* X, x_F > 0)$ (μb/nucleon)	90% C.L. limits
π^-	$2.71 \pm 0.33 \pm 0.11 \pm 0.13 \pm 0.11$	
π^+	$3.13 \pm 0.49 \pm 0.21 \pm 0.14 \pm 0.12$	
π	$2.84 \pm 0.27 \pm 0.10 \pm 0.13 \pm 0.11$	
K^-	$1.23 \pm 0.80 \pm 0.04 \pm 0.06 \pm 0.05$	$> 0.41, < 2.29$
K^+	$1.90 \pm 0.56 \pm 0.10 \pm 0.09 \pm 0.08$	
K	$1.67 \pm 0.46 \pm 0.07 \pm 0.08 \pm 0.07$	
p	$1.78 \pm 0.59 \pm 0.16 \pm 0.08 \pm 0.07$	

Table 8.11: D^* forward cross-sections, 250 GeV beam.

measurements reported in this and following subsections are adjusted where necessary to correspond to 94 PDG branching fractions; systematic errors (in which branching fraction errors are included) are changed accordingly.

Both D^+ and D^0 cross-section values have been published by most modern fixed-target experiments which address charm hadroproduction issues. Since the sum of these two species forms a significant fraction of the total charm cross-section,[8] these measurements can be used to assess the current state of theory. In Figs. 8.2 and

[8]Just what fraction of the charm cross-section might be comprised of D^+ and D^0 will be discussed later in this section.

B	$\sigma(BN \to DX, x_F > 0)$ (μb/nucleon)			
	D^+	D^0	D_s	D^*
π^-	$2.7 \pm 0.2 \pm 0.6$	$6.1 \pm 0.3 \pm 1.3$	$1.4 \pm 0.2 \pm 0.2$	$2.4 \pm 0.2 \pm 0.6$
	$(2.0\ ^{+0.5}_{-0.3} \pm 0.2)$	$(4.2\ ^{+0.6}_{-0.4} \pm 0.5)$	—	$(2.0 \pm 0.5 \pm 0.2)$
K^-	—	—	$2.3 \pm 1.2 \pm 0.5$	—
	$(4.7\ ^{+1.4}_{-1.0} \pm 0.5)$	$(5.0\ ^{+1.9}_{-1.1} \pm 0.5)$	$(5.8\ ^{+2.4}_{-1.4} \pm 1.0)$	$(2.9 \pm 1.4 \pm 0.3)$

Table 8.12: NA32 forward cross-sections, 230 (200) GeV beam [17,19].

8.3, we compare E769 results for π[9] and p-induced production of charm mesons (D^+, D^-, D^0, and $\overline{D}^0$) to results of previous experiments [17, 19, 2, 4, 12, 29, 30] as a function of beam energy. Also plotted are next-to-leading order (NLO) QCD predictions for the total charm plus anticharm particle forward cross-section; these are obtained by multiplying the $c\bar{c}$ cross-section, generated using the program of Mangano *et al.* [33], by a factor of 2 and requiring the c quark to have $x_F > 0$. HMRSB (SMRS2) parton distribution functions are assumed for target nucleons and beam protons (pions) [28], and theoretical parameters have been set to the default values used in [32]. An underestimate of the theoretical uncertainty has been obtained by varying the renormalization scale; other contributions, most notably those due to uncertainties in the charm quark mass and factorization scale, are expected to be at least as large [32]. If fragmentation is assumed to be constant as a function of energy, the energy dependence of D meson cross-sections can be directly compared to the theory for quarks; the agreement over the energy range shown appears reasonable.

In order to assess the accuracy of the NLO QCD central prediction for the total charm particle cross-section ($x_F > 0$), an estimate must be made of the fraction of the total cross-section accounted for by presently-measured species. Cross-section information on one further charm hadron is available, namely the lightest charm

[9] In the π beam plot, although all other experiments measure π^--induced production, E769's *combined* π beam result is used in order to maximize precision. The assumption implicit in this procedure, namely, that charm production is insensitive (at least at the level of E769 precision) to the charge of mesons impinging on a nuclear target, is discussed in Section 8.3.2.

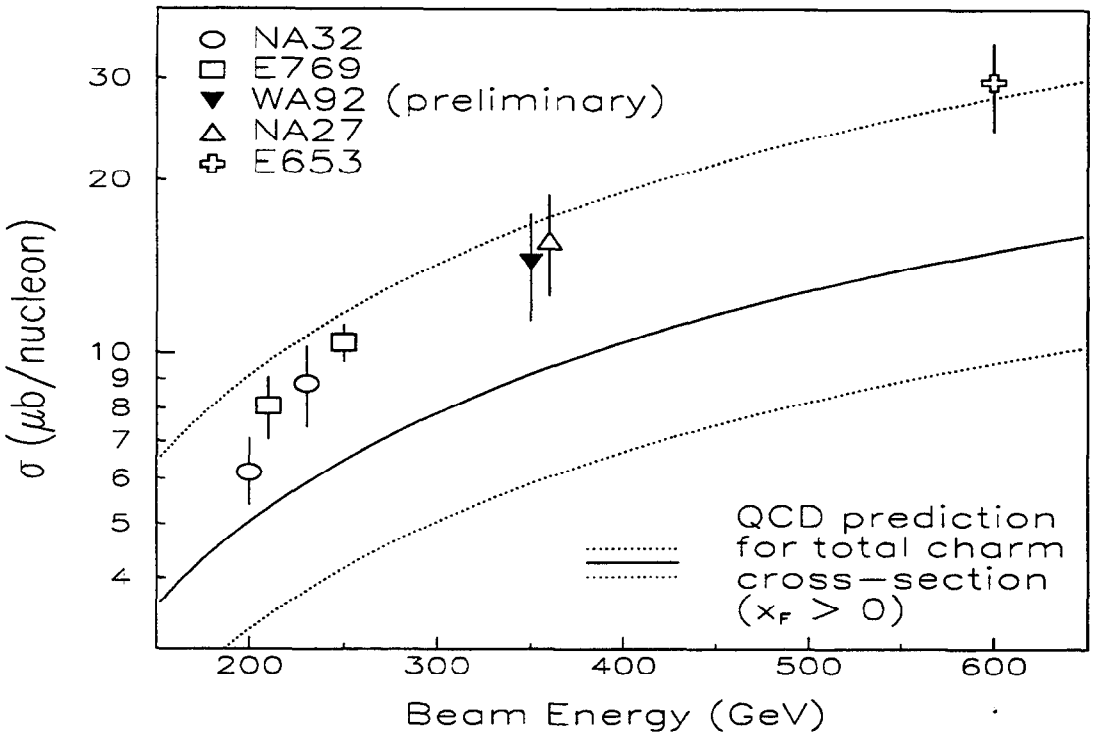

Figure 8.2: $\sigma(\pi N \rightarrow DX,\ x_F > 0)$, $D = D^+, D^-, D^0$, and $\overline{D}^0$. Measured values for E769 and previous experiments [17,19,2,29] compared to NLO QCD prediction [32] for total forward charm plus anticharm particle production. The band bordered by the dotted lines is an underestimate of the theoretical uncertainty in the central value represented by the solid line. Error bars include branching fraction uncertainty.

baryon Λ_c. In the same paper in which the forward cross-section results of this analysis are presented, a well-measured Λ_c cross-section (combined π beam) of $3.4 \pm 1.1 \pm 0.5$ μb/nucleon is given [10]. This value is consistent with that measured by NA32 with a 230 GeV π^- beam: $4.1 \pm 0.5 \pm 0.7$ μb/nucleon [18]. Weighted averages of π^- and π^+ beam results for the species D^+, D^0, D_s, and Λ_c and their antiparticles are summed in order to obtain our most precise partial measure of the charm plus anticharm particle cross-section ($x_F > 0$): $15.9 \pm 1.3 \pm 0.9$ μb/nucleon.

Forward production of Λ_c is evidently not suppressed with respect to D^+ at this energy. This and the significant D_s cross-section make it probable that undetected

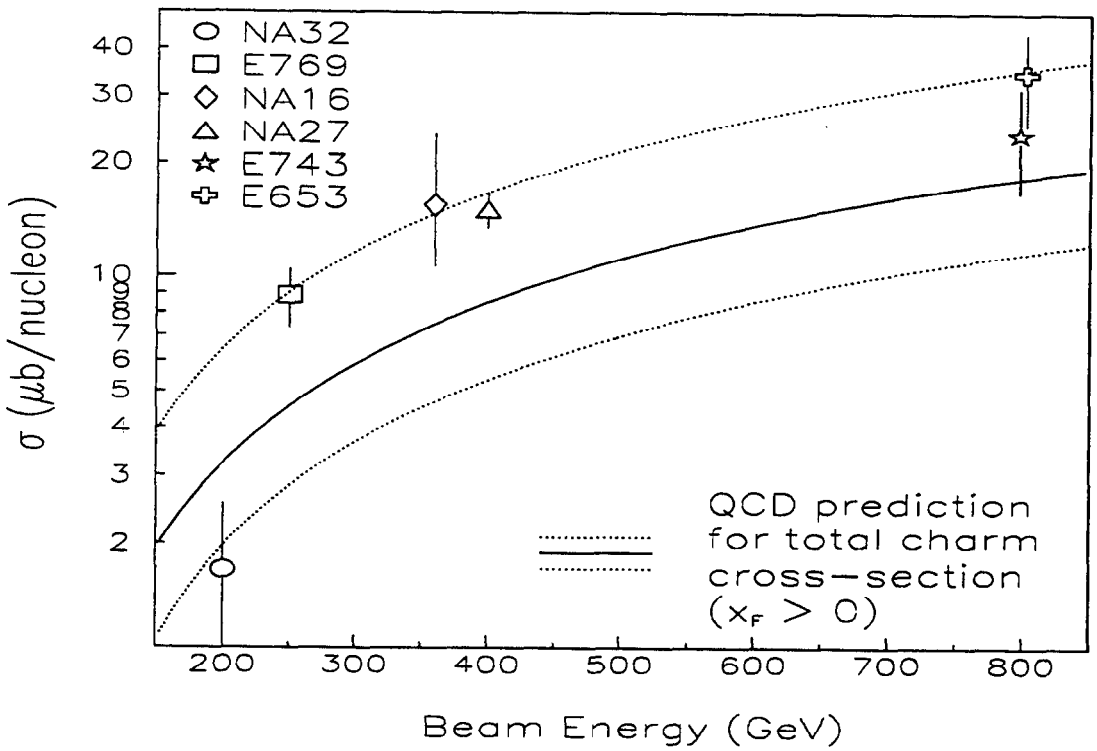

Figure 8.3: $\sigma(pN \to DX,\ x_F > 0)$, $D = D^+, D^-, D^0$, and $\overline{D}^0$. See explanation in Fig. 8.2 caption, replacing the references cited therein with [17,1,4,12,30]. Here, cross-sections shown for NA27 [4], E743 [12], and E653 [29] are 50% of values published for all x_F.

(including charm strange) baryonic species contribute appreciably to the total charm cross-section. Including an estimate for unseen charm species, it is evident that the NLO QCD central prediction for the total charm cross-section is low by about a factor of three. Given the huge latitude in normalization allowed by the current state of theory, however, this discrepancy is not particularly telling. It is interesting, nevertheless, to note that the $b\bar{b}$ cross-section predicted by QCD is also low compared with measurements [38].

8.3.2 Beam particle dependence

Before discussing the dependence of charm cross-sections on the three E769 beam species (π, K, p), we will justify the procedure of combining oppositely-charged meson beam results for purposes of comparison with results from previous experiments, which are obtained with π^- and K^- beams only. With its negatively and positively-charged mixed hadron beams, E769 is the first experiment to provide data (for both π and K) addressing this issue.

As discussed in Chapter 2, charm production at E769's energy is expected to be dominated (80% or more) by gg fusion, the balance coming primarily from $q\overline{q}$ annihilation. Since oppositely-charged mesons are charge conjugates of one another, specification of one set of parton distributions suffices to determine the other. Given the near u-d symmetry of the nuclear target (good to within a few percent), we do not expect between π^- and π^+ beams any significant difference in the hard-scattering amplitudes underlying charm production.[10] The situation with charged kaons is different, due to the replacement of d with s, the latter of which only contributes to the "sea" component of the target's parton distributions. The valence $\overline{u}$ quark of the K^- can annihilate with valence u quarks in the target, a mechanism not available in K^+-induced production. We therefore expect K^--induced cross-sections to be higher than those for K^+ by an amount on the order of 10%,[11] everything else being equal.

The only other likely mechanism for enhancement of production induced by one sign of beam meson over the other is the leading-particle effect (defined in Section 2.5). Measurements of this effect for different beam/charm meson combinations are given in Section 8.3.4. As a rough estimate, however, suffice it to say that in the forward hemisphere, the probability of hadronization to a leading charm meson is as much as 160% that for the non-leading antimeson. In this analysis, we combine leading and non-leading mesons (i.e., particle and antiparticle) into common signals, thereby

[10]The u-d mass difference is too slight compared to the available energy to have any measurable effect.

[11]The fraction of πN charm production attributable to $q\overline{q}$ annihilation is 20%. For the present estimate, however, we must subtract away "valence-sea" $q\overline{q}$ interactions. Assuming these latter occur with the $q\overline{q}$ probability predicted in pN charm production (10%), we obtain the rough prediction for K^- beam enhancement given in the text.

diluting this enhancement to the 15-30% level over the *neutral*-leading case and eliminating completely any discrepancy between charm particle cross-sections expected with beam particles of opposite sign.

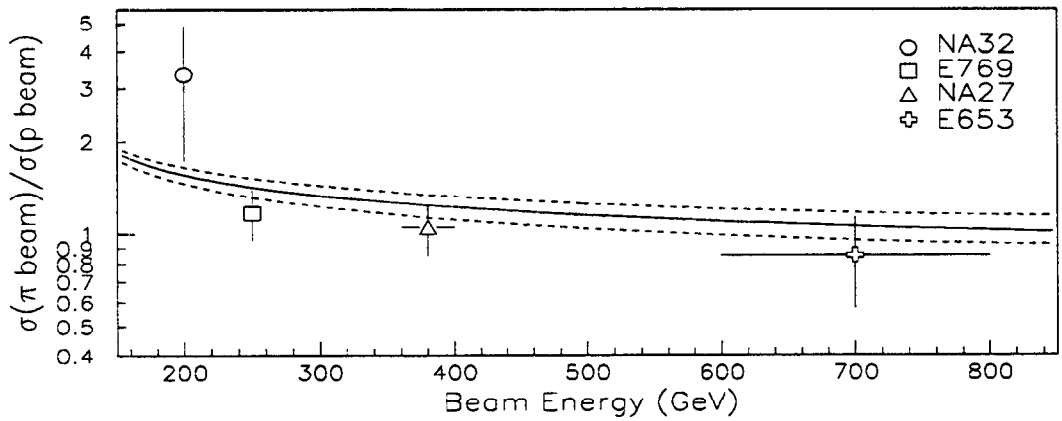

Figure 8.4: Ratio of $\sigma(\pi N \to DX,\, x_F > 0)$ to $\sigma(pN \to DX,\, x_F > 0)$ vs. beam energy (GeV), $D = D^+, D^-, D^0$, and $\overline{D}^0$. Measured values for E769 and previous experiments compared to NLO QCD prediction for total forward $c\bar{c}$ production (solid line). The band bordered by the dashed lines represents the theoretical uncertainty associated with parton distributions in the pion; an analogous uncertainty due to the proton should also contribute, but is not shown.

For π^- (K^+) beam, our most precise cross-section measurement for an individual charm species is at the 10% (15%) level. Therefore, any expected discrepancies should be indistinguishable from statistical fluctuations. It remains to be demonstrated, however, that no theoretically unexpected effects are at work. Our most precise measure of the π^-/π^+ beam cross-section ratio is obtained by summing D^+, D^0, and D_s mesons:

$$\frac{\sigma(\pi^- N \to DX,\, x_F > 0)}{\sigma(\pi^+ N \to DX,\, x_F > 0)} = 1.36 \pm 0.17 \pm 0.09. \tag{8.16}$$

For D^+ and D^0, the differences between π^- and π^+ beam cross-sections are only marginally significant, providing no compelling evidence of a physical effect.[12] For

[12] A lengthy search for a systematic cause, however, turned up nothing.

the kaon beams, the corresponding ratio is calculated without including D_s, which is not well-measured for K^-:

$$\frac{\sigma(K^-N \to DX,\ x_F > 0)}{\sigma(K^+N \to DX,\ x_F > 0)} = 1.09 \pm 0.26 \pm 0.04. \tag{8.17}$$

On the basis of this evidence (and the accompanying theoretical prejudice), combined π and K beam cross-sections are used for comparisons with previous measurements.

The total charm cross-section is expected to exhibit a significant dependence on beam, this sensitivity deriving in particular from the gluon momentum distributions of the interacting hadrons. As detailed in Chapter 2, this dependence can be expressed in terms of the first two moments of the beam particle gluon distribution, $<g>_{thr}$ and $<xg>_{thr}$, where the subscript indicates that the lower limit of integration is an effective charm threshold. Non-gg contributions to charm production must also be taken into account in predicting ratios of cross-sections for different beams. In this section we present ratios of forward charm particle plus antiparticle cross-sections, whose predicted values potentially differ from those for $\sigma_{c\bar{c}}$ due to two additional factors: forward-backward asymmetry in meson-nucleon hadroproduction and leading-particle enhancement. See Chapter 2 for a full discussion of these effects.

Comparing our measured forward cross-sections for different beams, no significant beam dependence in any of the individual D or combined pseudoscalar[13] cross-sections is found, suggesting that the average fractions of pion, kaon, and proton momenta carried by gluons above the charm threshold are at least comparable. In order to present our most precise measures of beam-particle dependence, we combine D^+ and D^0 results[14] for π, K, and p beams. These ratios are given in Table 8.13. Our π/K ratio is consistent with that obtained by NA32 at 200 GeV: $0.67\ ^{+0.14}_{-0.18}$ [17].

Well-measured parton distributions are available for the pion and proton, so a QCD prediction for the π/p cross-section ratio can be made. In Fig. 8.4, previous measurements[15] are compared to the theoretical prediction as a function of beam

[13] D^* cross-sections are not independent of those for D^+ or D^0 mesons, to which D^* decays strongly.

[14] p-induced D_s production is not well-measured.

[15] For the remainder of this chapter, measurements from other experiments are given without additional referencing. The reader is referred to the captions of Figs. 8.2 and 8.3.

B_1/B_2	$\frac{\sigma(B_1 N \to DX, x_F>0)}{\sigma(B_2 N \to DX, x_F>0)}$
π/p	$1.17 \pm 0.20 \pm 0.08$
K/p	$1.15 \pm 0.22 \pm 0.08$
π/K	$1.02 \pm 0.12 \pm 0.03$

Table 8.13: D forward cross-section ratios, $D = D^+, D^-, D^0$, and $\overline{D}^0$, 250 GeV beam.

energy. Horizontal error bars on the NA27 and E653 points reflect the fact that π^- and p beam measurements were made at different energies. Above 300 GeV, however, this ratio is expected to be relatively insensitive to beam energy. The data is consistent with the theoretical prediction, the measured π/p cross-section ratios following the expected decline with beam energy.

8.3.3 Hadronization

The total charm cross-section is the sum of cross-sections for all possible charm particles and antiparticles, divided by a factor to eliminate double-counting of $c\bar{c}$ pairs.[16] Cross-sections for all charm species, most notably charm baryons, have not yet been measured (or measured well). In connecting measured cross-sections to $\sigma_{c\bar{c}}$, it is therefore important to estimate the contribution of "missing" charm to the total. This requires knowing to what extent production of heavier charm hadrons is suppressed with respect to the "light" D^+ and D^0 mesons. As hadronization is a process that involves the exchange of many soft gluons, it cannot be treated in the context of perturbative QCD. Measurement of cross-section ratios for the lighter charm particles can at least provide experimental input for phenomenological models of hadronization (e.g., Monte Carlo fragmentation algorithms). In this section, we present cross-section ratio values and compare them to previous measurements.

Pseudoscalar D mesons are created either through hadronization of a charm quark or decay of a vector D^*; these processes are known as direct and indirect production,

[16]This factor would be exactly two if not for the existence of charmonium states.

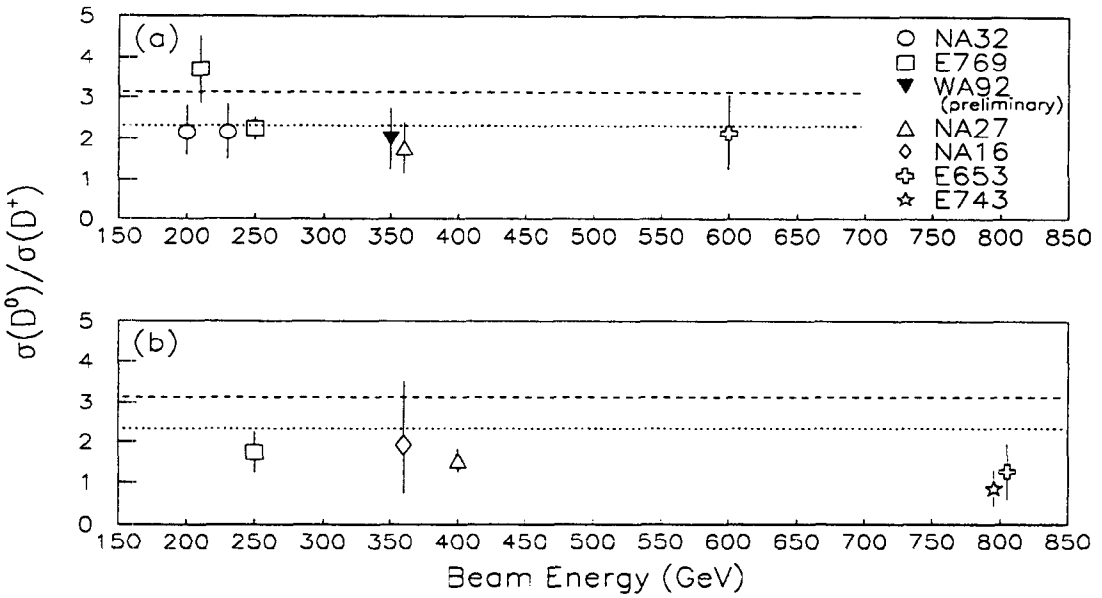

Figure 8.5: Ratio of $\sigma(BN \to D^0X,\, x_F > 0)$ to $\sigma(BN \to D^+X,\, x_F > 0)$ vs. beam energy (GeV) for (a) π and (b) p beams. Measured values for E769 and previous experiments compared to "simple-model" prediction (see text) assuming 94 (dashed) and 90 (dotted) PDG D^{*+} branching fractions.

respectively. By making two plausible assumptions, it is possible to predict the ratio of D^0 to D^+ cross-sections. First, we assume that $u\bar{u}$ and $d\bar{d}$ pairs are created with equal probability in the aftermath of a collision of high-energy hadrons. This implies that equal numbers of charged and neutral light D mesons will be produced. Second, we assume that hadronization to vector mesons (charged and neutral) is enhanced by a factor of three over corresponding pseudoscalar mesons. Since charged (neutral) D^*'s decay preferentially (exclusively) to D^0, the D^0 cross-section is expected to be higher than that for D^+.

In Fig. 8.5, measurements by E769 and previous experiments of the D^0/D^+ forward cross-section ratio are presented as a function of beam energy for π and p beams. Two "simple-model" predictions are given, corresponding to 94 and 90 PDG D^{*+} branching fractions. Interestingly, the data seems to conform much more closely

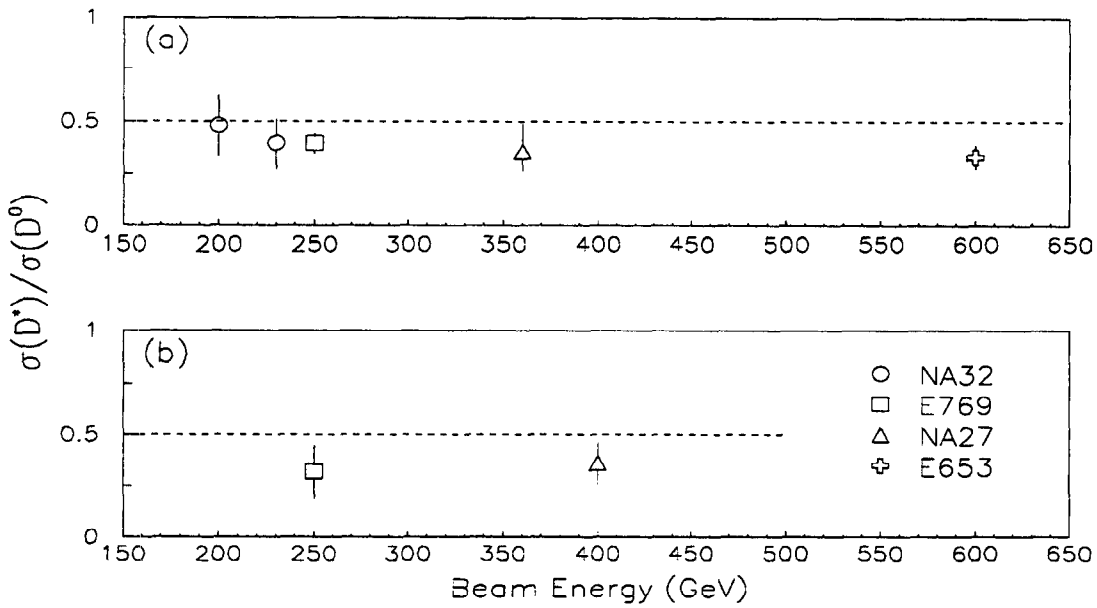

Figure 8.6: Ratio of $\sigma(BN \to D^{*+}X,\ x_F > 0)$ to $\sigma(BN \to D^0X,\ x_F > 0)$ vs. beam energy (GeV) for (a) π and (b) p beams. Measured values for E769 and previous experiments compared to "simple-model" prediction (see text) assuming 94 PDG D^{*+} branching fractions (dashed).

to the latter. The 94 PDG branching fractions for D^{*+} are dominated by a single set of measurements (1992 CLEO II). Assuming that these more recent branching fractions are accurate, one or both of the aforementioned assumptions might have to be discarded. The value of the D^0/D^+ cross-section ratio is much more sensitive to the charged/neutral ratio than to the vector/pseudoscalar ratio, making the former the more likely candidate for modification. In order to reach agreement with the general trend in π beam data, however, a charged/neutral (i.e., $d\bar{d}/u\bar{u}$) ratio of more than 1.5 must be assumed! Note that the p beam ratio is expected to be raised somewhat by higher leading-particle enhancement of D^0 over D^+. For neither π nor p beam is there any compelling evidence of energy dependence in the D^0/D^+ cross-section ratio.

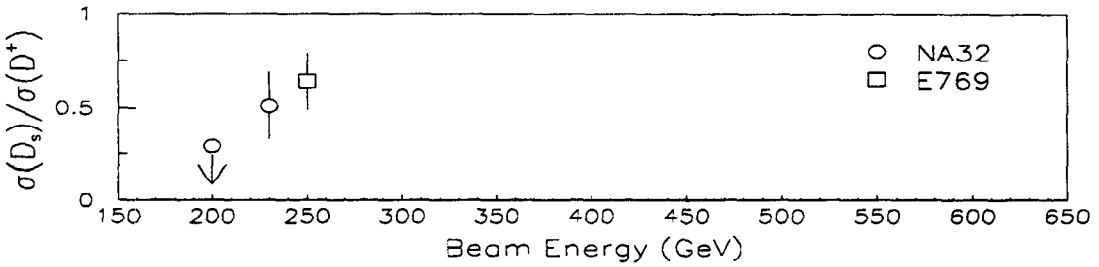

Figure 8.7: Ratio of $\sigma(\pi N \rightarrow D_s X, x_F > 0)$ to $\sigma(\pi N \rightarrow D^+ X, x_F > 0)$ vs. beam energy (GeV). Measured values for E769 and NA32.

The assumptions discussed above also lead to a prediction for the D^{*+}/D^0 cross-section ratio. In Fig. 8.6, E769 and previous measurements of this quantity are presented for π and p beams. Unlike the D^0/D^+ ratio, the ratio of D^{*+} to D^0 is not particularly sensitive to the D^{*+} branching fractions assumed; therefore, only the simple-model prediction assuming 94 PDG values is plotted. The data for both beams tends to fall significantly below the expected ratio. Only the p beam ratio should be affected (in this case, lowered) by differential leading-particle enhancement. Interestingly, these measured values of the D^{*+}/D^0 cross-section ratio (which is also sensitive to the charged/neutral ratio) favor a charged/neutral ratio of around 0.7, a change in the direction opposite to that indicated by the D^0/D^+ ratio. It seems evident that some modification must be made to the simple model used in making these predictions, such as allowing the vector/pseudoscalar ratio to differ in the charged and neutral D cases.

In Fig. 8.7, we present a final cross-section ratio, namely D_s/D^+. As these mesons are identical except for the replacement of a d by an s quark, this ratio gives a measure of the suppression of the heavier quark's production at this energy. In interpreting this ratio, however, it should be recalled that only about one third of D^{*+}'s decay to D^+ while all D_s^*'s decay to D_s.

Beam	Particle	Leading flavor(s)	A
π	D_s	none	-0.11 ± 0.07
K	D^+	none	-0.11 ± 0.07
	D^0	u or none	-0.19 ± 0.06
	D_s	s	0.25 ± 0.11
p	D^+	d	0.18 ± 0.05
	D^0	u or d	0.06 ± 0.06
	D_s	none	-0.10 ± 0.17
	D^*	d	0.36 ± 0.13

Table 8.14: Leading particle asymmetries ($x_F > 0$). Statistical errors are shown; systematic errors are negligible. For beam/particle combinations for which the leading-particle effect is undefined (neutral-leading case) or diluted by indirect production (K beam, D^0), the asymmetry is defined as that between particle (containing c) and antiparticle (containing $\bar{c}$), irrespective of beam particle charge.

8.3.4 Leading-particle asymmetries

One aspect of hadroproduction which cannot be treated perturbatively is the leading-particle effect, which is defined and discussed in Chapter 2. The size of this effect is usually quantified as a leading-particle asymmetry A, defined as

$$A \equiv \frac{\sigma(\text{leading}) - \sigma(\text{nonleading})}{\sigma(\text{leading}) + \sigma(\text{nonleading})}, \tag{8.18}$$

where $\sigma(x)$ is the forward cross-section for x particles. Since the absolute normalization cancels out in this quantity, the cross-sections σ can be calculated as simply the number of x events divided by the acceptance, as a function of x_F, integrated over $x_F > 0$. This binwise calculation is important because A has been measured to have a strong dependence on x_F [8]. Measured values of A for production of various charm particles for K and p beams are shown in Table 8.14.

The asymmetry induced by a leading s quark is found to be consistent with that of the lighter quarks. These A values should be compared with our previously-published

π beam results, $A_{D^+} = 0.18 \pm 0.06$, $A_{D^0} = -0.06 \pm 0.07$, and $A_{D^*} = 0.09 \pm 0.06$ [6, 9].[17]

[17]The D^+ and D^0 results are obtained with π^- beam data only. The latter is diluted by indirect production.